OFFICE OF NAVAL RESEARCH

Contract No. N00014-91-J-1409

Technical Report No. 153

Sensitivity of Electrochemical Adlayer Structure to the Metal Crystallographic Orientation: Potential-Dependent Iodide Adsorption on Au(100) in Comparison with Other Low-Index Surfaces

by

Xiaoping Gao, Gregory J. Edens, Fan-Chen Liu, and Michael J. Weaver

Prepared for Publication

in

Journal of Physical Chemistry

Department of Chemistry

Purdue University

West Lafayette, Indiana 47907-1393

February 1994

ABSTRACT

The potential-dependent ordered atomic structures formed for iodide adsorption on Au(100) from dilute aqueous alkali iodide electrolytes as discerned by means of in-situ scanning tunneling microscopy (STM) are reported and compared to the corresponding behavior of the other two low-index faces, Au(111) and (110). As in related studies, emphasis is placed on linking the microscopic structural information to the voltammetric and other macroscopic electrochemical response, including the use of "potentiodynamic" STM tactics where real-space images are acquired during appropriate electrode potential steps or sweeps. While relatively low iodide coverages, $\theta_I \sim 0.1$, are sufficient to lift the hexagonal Au(100) reconstruction, yielding large ordered (1 × 1) domains by ca -0.6 V vs SCE, ordered iodide adlayers are formed only above -0.2 V. A compressible incommensurate ($2\sqrt{2} \times p\sqrt{2}$) phase ($\theta_I \approx 0.46 - 0.49$) is observed between ca -0.2 and 0 V, which reverts to a distinct ($2\sqrt{2} \times \sqrt{2}$)R45° structure ($\theta_I = 0.5$) featuring uniform binding in twofold bridging sites. Interestingly, while the latter structure is retained locally at higher potentials, it is interspersed with narrow (3-4 atom wide) strips having a rotated hexagonal pattern. The latter becomes increasingly dense, and eventually dominant, towards higher potentials. This microscopically nonuniform (or "spatially modulated") phase is noteworthy as well as unusual; the corresponding iodine phases on Au(111) and (110) display, as is common, structural uniformity at a given potential. A related distinction concerns the potential-induced phase transitions: while they display sharp first-order behavior on Au(111) and (110), the phase transformation on Au(100) is diffuse. These microscopic-level differences in the adlayer phase structure and dynamics as seen by STM are also reflected in the macroscopic behavior as discerned by cyclic voltammetry and ac impedance measurements. Nevertheless, closely similar surface concentration-potential (Γ-E) behavior is seen for the ordered adlayers on all three low-index gold surfaces. The various adsorbate-adsorbate interatomic forces responsible for the observed potential-induced adlayer compressibilities are briefly outlined.

Chemisorption of atoms or molecules on monocrystalline metal surfaces characteristically yields ordered adlayer structures.[1] This ordering can be understood in general terms from an interplay between the preference for adsorbate bonding in specific coordination sites and the dominant presence of adsorbate–adsorbate interactions at higher coverages. Examination of such adsorbate structuring, once the exclusive preserve of metal surfaces in ultrahigh vacuum (uhv), has more recently been broadened to embrace electrochemical interfaces. Initially, such information for the latter systems was obtained by electrode emersion and transferral into uhv, with subsequent analysis by low-energy electron diffraction (LEED) or related uhv-based techniques.[2] Such "ex-situ" tactics remain important, along with related approaches involving preparation of electrochemical interfaces in uhv by gas-phase dosing.[3]

Nevertheless, a major advance over the last few years is the development of methods capable of yielding atomic-/molecular-level information on spatial surface structure for in-situ electrochemical interfaces under potential control at a level of sophistication that is on a par with (or even beyond) that attainable in uhv.[4] Probably most notable has been the almost concurrent emergence of in-situ scanning tunneling microscopy (STM) and synchrotron-based surface X-ray scattering (SXRS).[4,5] These methods, while having notably different strengths and weaknesses, can yield in suitable cases remarkably detailed yet complementary information on potential-dependent adlayer as well as substrate structure.[4] A recent focus in our laboratory is concerned with utilizing STM for the exploration of potential-dependent atomic structure and related dynamics on various monocrystalline gold-aqueous interfaces. Particular attention has been devoted to elucidating the charge-induced formation and removal of reconstruction which occurs on all three low-index and some high-index gold faces,[6-8] and the ordered anion adlayer structures that form at higher

potentials, most characteristically in halide media.

In the latter case, we have selected for detailed study iodide adsorption on the three low-index faces.[4,10-12] One virtue of this choice is that remarkably accurate as well as detailed iodide adlayer structures on Au(111) and (110) electrodes have recently been deduced by means of SXRS by Ocko et al.[13] Each of these systems exhibit an interesting sequence of potential-induced phase transitions associated with the iodide-induced removal of the substrate reconstruction, yielding large uniform (1 × 1) terraces, followed by the formation of multiple ordered iodide adlayer phases at higher potentials where the coverage approaches within ca 20-25% of the anticipated close-packed limit. We describe in a companion paper[11] the particularly rich behavior of the Au(110)-I^- system, which displays additional ordered alkali cation/iodide coadsorbed phases and also a new type of long-range substrate restructuring at high potentials.[14] As exemplified in our earlier examination of the Au(111)-I^- system,[10] and particularly in studies of charge-induced reconstruction on Au(100)[6c,d] and Au(110),[8b] the accurate assignment of STM structural patterns as well as information on phase-transition dynamics can be facilitated greatly by image acquisition *during* electrode potential sweeps or steps. This tactic, dubbed "potentiodynamic" STM, also provides an invaluable link with the corresponding macroscopic electrochemical phenomena as divulged by cyclic voltammetry and related methods.[11]

Reported in the present article are atomic-resolution STM and electrochemical data of this type for iodide adsorption on Au(100). The system features some intriguing variations in the adlayer packing arrangements even within a given substrate terrace. In the wake of our related electrochemical STM studies of the corresponding Au(111)[10] and Au(110)[11] systems, we also undertake here a comparison of the potential-dependent structural and dynamical phase

behavior of ordered iodide adlayers on all three low-index gold surfaces. Included in this exercise are corresponding cyclic voltammograms and ac impedance-potential data, which when combined with the potentiodynamic STM results reveal an interesting interplay between iodide adlayer structure and dynamics and the substrate atomic template. We also consider briefly the nature of the interatomic interactions that control the packing densities and potential-induced compressibility of the adlayer structures.

EXPERIMENTAL SECTION

The experimental STM procedures are largely as described in earlier reports.[6] The microscope is a Nanoscope II (Digital Instruments) equipped with a bipotentiostat for electrochemical STM. The STM tips were 0.01 inch tungsten tips etched electrochemically in 1 M KOH, and insulated with either clear nail varnish or a thermosetting polyethylene plastic. Most STM images were obtained in the so-called "height mode" (i.e., at constant current). The monocrystalline gold surfaces (hemispheres, 5 mm diameter) were prepared at LEI-CNRS, Meudon, France, by Dr. A. Hamelin. They were pretreated by flame annealing and cooled partly in air and then in ultrapure water immediately before transferring to the STM (or conventional electrochemical) cell.[19] The counter electrode was a gold wire, and the quasi-reference electrode was a platinum wire. All electrode potentials quoted here, however, are converted to the saturated calomel electrode (SCE) scale. The electrolyte used for the STM experiments was usually 10 mM KI. The cyclic voltammetric data shown here were obtained in a conventional electrochemical cell. The ac impedance measurements employed a 10 mV ac signal (20 to 400 Hz) with phase-sensitive detection using a PAR Model 5204 lock-in amplifier, along with a PAR 173/179 potentiostat.

RESULTS AND DISCUSSION

Similarly to our companion article on Au(110),[11] it is instructive to first examine the nature of the cyclic voltammetric response of Au(100) in the iodide media employed here, under conditions that correspond at least roughly to those utilized in the STM experiments described below. As noted for Au(110),[11] the occurrence of potential-induced phase transitions as identified in most cases by potentiodynamic STM is typically signaled by voltammetric (i.e., current-potential) features arising from the (nonfaradaic) redistribution of electronic charge. Prompted by our intention here to intercompare the behavior of all three low-index gold surfaces, Fig. 1A-C shows voltammograms obtained at 10 mV s^{-1} on Au(111), (100), and (110), as indicated, in 50 mM $KClO_4$ + 5 mM KI. (As expected, the voltammetric features are insensitive to the presence of the $KClO_4$ supporting electrolyte, as well as the iodide concentration. The former is included to diminish the solution resistance.) The potential excursion, -1.0 to 0.25 V vs. SCE, is selected so to encompass the various phase transitions and related features of significance here. Included on a common potential scale with the voltammograms are differential capacitance-potential (C_d - E) curves, obtained from ac impedance measurements at 23 Hz. For clarity, the C_d values are plotted on a fourfold more sensitive y-axis scale than the voltammograms. (Note that the voltammetric current axis can also be considered as a capacitance scale at a given sweep rate under circumstances, as are essentially encountered here, where only nonfaradaic processes occur.)

Although perhaps not immediately evident to the casual observer, there are several features on all three voltammograms that signal the occurrence of specific phase transitions. Most prominent, at least on the positive-going potential traces, are current peaks labelled here b, which are partnered on the negative-going traces by less pronounced features marked b'. As shown most

clearly by potentiodynamic STM measurements, e.g. for Au(100)[6d] and Au(110),[8b,11] the b and b′ features signal the removal and reformation, respectively, of substrate reconstruction. This process is particularly interesting (and well-studied) for Au(100), featuring a hexagonal to square-planar substrate structural change, incurring substantial metal mass transport.[6] While at least the (1 × 1) → hex potential-induced transition in nonadsorbing (such as perchlorate) electrolytes is sluggish ($\tau_{\frac{1}{2}}$ ~ 10 min), both directions of the (1 × 1) ⇌ hex conversion can become extremely facile ($\tau_{\frac{1}{2}} \lesssim 1$ s) in iodide media under comparable potentiodynamic conditions.[6d] This dramatic effect upon the reconstruction dynamics can be rationalized on the basis of the marked acceleration of the gold surface mobility seen to be engendered by iodide adsorption.

The initial occurrence of iodide adsorption can most readily be discerned from the rising portion of the C_d–E curves; for Au(100) this is seen to occur at about −1.0 V (Fig. 1B). A rough thermodynamic analysis of families of C_d–E traces at varying iodide concentrations indicates that the fractional iodide coverage, θ_I, is about 0.1 at the onset of the hex → (1 × 1) transition. The iodide coverage increases significantly as the reconstruction is lifted towards positive potentials, as gleaned from the large positive charge (i–E spike) on the voltammogram. Noteworthy, however, is the virtual absence of a corresponding C_d–E response corresponding to b/b′ on all three faces (Fig.1). This indicates, as might be expected from the voltammetric hysteresis, that the hex ⇌ (1 × 1) transition is not reversible under the usual low-amplitude (10 mV p-p) oscillatory conditions, at least not at the lowest frequency (10 Hz) employed. The same conclusion also applied when larger potential oscillations (up to 100 mV) were employed.

Two types of voltammetric features are observed at higher potentials, both associated with the formation of adlayers. The first type, labelled c/c′ in Fig. 1, is somewhat dependent on the nature of the supporting electrolyte cation. This effect is most clearly seen for Au(110), where ordered adlayer images are observed in cesium iodide, consistent with the presence of a coadsorbed mixed cation/anion phase.[11] The morphology of the c/c′ transition on Au(110), marking the dissipation of the film towards higher potentials, is also notably different in K^+ and Cs^+ electrolytes.[11] The c/c′ features on Au(100) and especially Au(111) are also significantly, though more subtly, dependent on the alkali cation. Thus for Au(100), c/c′ appears at ca 50 mV higher potentials in Cs^+ than in K^+ electrolytes. However, no mixed cation/anion adlayers could be discerned by STM on Au(100) and (111), presumably because of their more mobile and/or disordered nature compared with Au(110).

The second type of voltammetric contour, of central concern here, consists of those appearing at higher potentials than c/c′, marked d/d′ and e/e′ in Fig. 1. The microscopic origin of these features as deduced by potential-dependent STM data is discussed in detail below. It is worth commenting briefly at this point on the behavior of these various transitions as they appear voltammetrically in comparison with the corresponding C_d–E data. While the c/c′ (cation-sensitive) transition is sensed in each case by the ac impedance measurements (Fig. 1), the higher-potential transitions d/d′ and e/e′ are insufficiently rapid and reversible to be detected in this manner (vide infra). Impedance measurements undertaken over a range of frequencies, from 10 to 500 Hz, showed that the former, cation-sensitive, transitions were attenuated only above ca 200 Hz. This finding testifies to their remarkably reversible nature, the formation/removal of the mixed cation/anion adlayer thereby exhibiting relaxation times around 10^{-2} s.

Potential-Dependent Iodide Adlayers on Au(100)

As already noted, of particular interest here is the positive potential region, above ca -0.2 V, where ordered iodide adlayers are observed by STM. As for Au(110),[11] we are interested in comparing the potential-induced formation of distinct iodide adlayer patterns in comparison with the voltammetric response. Three distinct iodide adlayers can be discerned in this high potential region. The first type, labelled here "adlayer I", appears when the potential is swept or stepped above the voltammetric feature d/d′. Figure 2A shows a representative potentiodynamic STM image that illustrates this adlayer pattern in relation to the substrate structure. The bottom one-third of this upward-rastered image was obtained with the electrode potential held at -0.25 V. A square-planar array of dots (i.e., tunneling maxima) are observed, each separated by a distance, 2.9 ± 0.2 Å, consistent with the presence of an unreconstructed, i.e. (1 × 1), Au(100) substrate. Similar images can indeed be obtained throughout the potential region bounded by b/b′ and d/d′. As for other systems, the presence of even substantial adsorbate coverages can commonly yield only substrate images when the adsorbate is mobile and/or disordered.

A dramatic change in the imaged pattern is seen, however, immediately after stepping the potential to -0.1 V (i.e., just above d/d′), corresponding to the upper two-thirds of Fig. 2A. A near-hexagonal array of spots in now seen, with nearest-neighbor spacings between 4.2 and 4.6 Å, consistent with the presence of an ordered iodide (or monoatomic iodine[15]) adlayer. Following similar arguments as for Au(111)[10a] and Au(110),[11] such "composite-domain" images can provide detailed and surprisingly accurate information on the adlayer real-space structure, including the adsorbate-substrate registry. The basic tactic involves mutual extrapolation of the juxtaposed adlayer and substrate domains. Since the geometry of the latter is known accurately, the procedure can largely circumvent

errors arising from thermal drift and related x-y distortions in the STM images.

On this basis, the adlayer structure I can readily be seen to contain parallel rows of iodine atoms lying along the $\sqrt{2}$ direction (i.e., 45° to the substrate rows). The straight line shown in Fig. 2A is drawn along this direction so to lie atop each diagonal gold atom, as discerned from the lower segment of the image. Also evident from this extrapolated line (and many others, not drawn) is that the $\sqrt{2}$ iodine rows are spaced evenly, each being spaced $\sqrt{2}$ (i.e., 4.08 Å) apart. As in other examples,[10,11] additional information on the adsorbate binding sites can be obtained from the observed periodic variations in the z-corrugations ("moiré pattern"), given that for iodine (and some other simple adsorbates) the z-displacement anticipated geometrically are at least qualitatively evident in the images. Thus atop-coordinated adsorbate, in particular, appears "brighter" than that bound in multi-fold sites. This supposition can indeed be confirmed readily by inspecting Fig. 2A, where the "brightest" iodine atoms situated close to the domain edge are clearly seen to be in registry with substrate atoms, thus being bound in atop sites.

An interesting feature of the adlayer I pattern involves periodic undulations of z-corrugation ("spot intensity") along the $\sqrt{2}$ direction, being repeated every 11 atoms or so. Across the $\sqrt{2}$ direction, an alternating "bright - dark" pattern is observed. The long-range periodicity is seen more clearly in Fig. 2B. While the substrate has a similar x-y orientation in Fig. 2A and B, the moiré pattern of the latter is rotated by 90°, indicative of the presence of another rotational domain. Clearly evident is a long-range "interference" pattern featuring "ridges" (brighter segments) spaced alternately across, but not necessarily perpendicular to, the $\sqrt{2}$ direction. An approximate real-space ball model consistent with these observations is depicted in Fig. 3A. The rectangular cell features a short, essentially fixed $2\sqrt{2}$ dimension, with the longer

direction, designated generally p$\sqrt{2}$, having some compressibility, thereby yielding a (2$\sqrt{2}$ × p$\sqrt{2}$) unit cell. The latter direction exhibits longer periodic variations in binding site, from atop to fourfold hollow back to atop in the unit cell as shown.

Indeed, while p ≈ 11–12 in Fig. 2A, in approximate accordance with the structure drawn in Fig. 3A, images obtained at slightly higher potentials yield considerably larger p values, in the range 11–25. This point is exemplified in the large-scale images shown in Fig. 2C and D, obtained at slightly (ca 0.05 V) higher potentials than for Fig. 2A. Significantly, this alteration in unit-cell distance provides accurate information on the potential-induced adlayer compressibility, in that slight (few percent) diminutions in the interatomic spacing along the p$\sqrt{2}$ direction result in marked *increases* in the "wavelength" of the periodicity, i.e., the unit-cell length. Thus in Fig. 2C and D, p ≈ 20 and 25, respectively; these patterns correspond to iodide coverages, θ_I, of 0.475 and 0.481, to be compared with θ_I = 0.458 when p = 11 (as in Fig. 2A).

Further compression along the p$\sqrt{2}$ direction should ultimately yield iodine adlayer strings with each atom having an essentially invariant binding site (i.e., p → ∞); such a structure would more economically be described by a (2$\sqrt{2}$ × $\sqrt{2}$) unit cell. Such a further uniaxial compression down to a $\sqrt{2}$ interatomic spacing is indeed achieved by small additional increases in potential, by ca 0 V vs. SCE. Interestingly, however, a concomitant lateral shift in the $\sqrt{2}$ iodine row position occurs, so that *all* the iodines are now situated in twofold bridging sites, with θ_I = 0.50. The ball-model structure for this (2$\sqrt{2}$ × $\sqrt{2}$) unit cell, also labeled here "adlayer II", is shown in Fig. 3B; comparison with the (2$\sqrt{2}$ × 11$\sqrt{2}$) pattern in Fig. 3A shows that the $\sqrt{2}$ rows running from the top left to bottom right of the lattice as shown are shifted diagonally across into twofold sites in Fig. 3B.

Again, such a degree of adlattice detail is deduced from potentiodynamic STM images that feature a suitable structural transition triggered during data acquisition. Figure 4A shows such an example, involving a potential step similar to that in Fig. 2A, but now from -0.25 V to 0 V so to generate the $(2\sqrt{2} \times \sqrt{2})$ adlayer. The line drawn along the "atop substrate" direction lies in between adjacent iodine rows, in harmony with the real-space ball model in Fig. 3B. Also consistent with this picture is the observed uniform z-corrugation given that *all* the iodine atoms occupy equivalent binding sites in Fig. 3B. Noteworthy are the interatomic distances for the $(2\sqrt{2} \times \sqrt{2})$ structure: 4.08 Å along the $\sqrt{2}$ direction and 4.56 Å along the two diagonal iodine rows. The former distance indicates significant compression, being *smaller* than the effective van der Waals iodine diameter, 4.3 Å[17] (vide infra).

As expected, both rotational domains of the $(2\sqrt{2} \times \sqrt{2})$ adlattice are observed, sometimes on the same substrate terrace. Figure 4B shows such an example. An interesting additional feature is the presence of a substrate screw dislocation in the middle-lower region of Fig. 4B, showing the resulting distortion of the iodine adlattice. Another structural mutation of this "adlayer II" is shown in Fig. 4C. Uniform regions of the $(2\sqrt{2} \times \sqrt{2})$ adlayer are seen to be interrupted periodically by parallel "channels" lying along one of the directions diagonal to the $\sqrt{2}$ rows. The iodines within these strips are apparently more mobile along the row direction, appearing as streaks. Note that the $(2\sqrt{2} \times \sqrt{2})$ domains either side of these strips are displaced laterally by half the distance between adjacent $\sqrt{2}$ rows (2.05 Å), i.e., with the iodine atoms bound in the complementary set of twofold bridging sites available on the Au(100) substrate. This mutation illustrates the ease by which sets of iodine atoms can move collectively between adjoining $\sqrt{2}$ sites.

The $(2\sqrt{2} \times \sqrt{2})$ structure is reproducibly observed only within a narrow

potential region, about 0 to 0.1 V. At higher potentials, corrugated structures again become apparent. Figure 4D is another composite-domain image showing such an example, involving a potential step from −0.25 V to 0.3 V during the upward-rastered data acquisition. Careful examination of such patterns, labelled here collectively "adlayer III", show the adlayer to be rotated by about 5° from the $\sqrt{2}$ direction, consequently exhibiting a periodic alteration of the binding sites so to yield the observed z-corrugation. A ball model that approximates such an adlayer pattern is shown in Fig. 3C. Note that each iodine row lying close to (displaced 5° from) the $\sqrt{2}$ direction yields periodic atop binding, every eighth iodine, matching the image in Fig. 4D. The iodine coverage in Fig. 3C is essentially 0.50 as is the $(2\sqrt{2} \times \sqrt{2})$ structure in Fig. 3B. The row rotation for the former, however, alters the iodine row angles so to approach hexagonal packing more closely. Correspondingly, the interatomic spacing along the "near-$\sqrt{2}$" direction is increased slightly, to 4.33 Å.

Surprisingly, however, potential excursions within the region, ca 0.1 to 0.25 V, bordered by adlayers II and III yielded iodine patterns that exhibit flexible superstructures containing local atomic arrangements periodically characteristic of *both* adlayers II and III. A pair of detailed atomic-resolution images illustrating such heterogenous patterns are given in Figs. 5A and B. The former, obtained at 0.2 V, displays domains having a uniform $(2\sqrt{2} \times \sqrt{2})$ structure separated by narrow linear regions, running diagonally to the $\sqrt{2}$ direction. These strands feature marked, even jagged, z-corrugations reminiscent of the rotated adlayer domains seen more uniformly in Fig. 4D. The other example, Fig. 5B, show a similar periodic "spatial modulation" (cf ref. 18), but with the "z-corrugated" strips containing typically one extra atom across than in Fig. 5A.

An intriguing additional aspect of such local phase coexistence is revealed in large-scale images such as Fig. 5C, also obtained at 0.2 V. Clearly evident

is a distinctly *nonuniform*, yet stable, pattern, containing not only both (ca 60°) rotated domains, but also considerable variations in the separation between the interconnected "z-corrugated" strands. Such reproducibly variable patterns indicate the ability of this adlayer system to yield locally varying, yet apparently equilibrated, unit-cell patterns. A clue to the apparent stability of these nonuniform structural patterns is contained in Fig. 5D, referring to the same imaged area as Fig. 5C, but obtained about 1 min after lowering the potential to 0 V. Although the uniform $(2/2 \times /2)$ iodine domains are essentially unchanged from before, the corrugated strands have almost disappeared, yet remaining are numbers of small surface defects. This infers that the formation of the locally non-uniform z-corrugated strands is accompanied by distortions in the underlying substrate lattice, which in turn may "lock in" a particular initially formed adlayer arrangement.

Potentiodynamic Adlayer Transitions on Au(100)

Having identified the nature of the potential-dependent iodine adlayer structures on Au(100), as discussed in the preceding article[11] an interesting issue involves the dynamics of the phase interconversions. An instructive approach for this purpose is to acquire sequences of potentiodynamic STM images under potential sweep conditions that match the voltammetric data. As demonstrated for Au(110), the voltammetric features e/e′ can be identified clearly as arising from a transition between a pair of discrete, yet compressible, iodine adlayer structures.[11] Given that the Au(100)-I^- system also exhibits distinctly potential-dependent iodine adlayer arrangements, it is of interest to examine in comparative fashion the corresponding voltammetric and potentiodynamic STM data.

The left-hand side of Fig. 6 shows a pair of voltammograms obtained at 5

and 50 mV s^{-1} (dashed, solid traces, respectively) for Au(100), and also (111) and (110) as indicated, over a suitably narrow potential range so to encompass only the adlayer transitions e/e′ themselves. (While the voltammograms in Fig. 1 also contain these features, the details are shown more clearly along with the sweep-rate dependence in Fig. 6.) The right-hand side of Fig. 6 shows the corresponding C_d–E profiles, obtained at 23 Hz with a 5 mV s^{-1} potential sweep. As noted above, the ac impedance is seen to be largely non-responsive to the e/e′ transitions, although the data provide useful information on the "fixed-coverage" capacitance, and hence dielectric, properties of the ordered adlayers themselves.

Figure 7 consists of examples of potentiodynamic STM data for Au(100) in 10 mM KI that shed light on the microscopic phenomena responsible for the corresponding voltammetric features seen in Fig. 6. The first image, Fig. 7A, was obtained for a single (25 × 25 nm) terrace region while sweeping the potential from 0.1 to 0 V during the downward-rastered data acquisition. The voltammetric current is featureless over this potential range (Fig. 1). As expected, the upper part of the image shows a "spatial modulation" structure (adlayer III) as discussed above. By the lower part of the image (corresponding to 0.05 V), however, the z-corrugated strips become sparse, a more uniform ($2\sqrt{2}$ × 2) structure increasingly prevailing. The next image, Fig. 7B, was obtained for the same surface region, but now rastered upward, while the potential was swept between −0.02 and 0.12 V. Note that the z-corrugated strips, diagnostic of adlayer III, have now disappeared. In addition, a disordered region is evident starting at about two-thirds up the image (ca −1.0 V), corresponding to the onset of the voltammetric peak e′ in Fig. 6. The following downward-rastered image, Fig. 7C, was acquiring while the potential was swept from −0.12 to −0.22 V. The upper portion shows a pattern reminiscent of adlayer I, but without the clearcut z-corrugations evident in some equilibrium images obtained at similar

potentials (e.g. Fig. 2A-D). Two-thirds down the image, by about -0.18 V, this adlayer disappears (within 5-10 mV), being replaced by essentially a substrate pattern, although the latter is masked somewhat by the apparent presence of disordered adsorbate. This adlayer order-disorder transition therefore corresponds to the voltammetric feature d' (Fig. 6).

Retracing the potential at 5 mV s^{-1} from -0.2 to -0.1 V, indeed, reforms the adlayer I pattern ($2\sqrt{2} \times p\sqrt{2}$) at about -0.13 V, coinciding with the voltammetric peak d. Further increases in potential yield a gradual transition towards the ($2\sqrt{2} \times \sqrt{2}$) (adlayer II) pattern. The reformation of adlayer III, however, does not occur until about 0.02 to 0.1 V, as seen in the upward-rastered image shown in Fig. 7D, acquired from 0 to 0.1 V. Comparison between Fig. 7A and 7D, referring to the same potential region but for negative- and positive-going potential sweeps, emphasizes the hysteresis involved in the adlayer II/III transitions. However, these transformations are somewhat "diffuse", occurring in a semi-continuous fashion with respect to potential and time as well as iodine coverage. This behavior matches the broad ill-defined nature of the e/e' voltammetric transition (Fig. 6).

Comparison with Iodine Adlayers on Au(111), Au(110), and Related Surfaces

It is useful at this point to intercompare the nature of the potential-dependent iodine adlayer structures and phase transitions observed on Au(100) with the corresponding behavior on the other two low-index gold faces. The somewhat "diffuse" nature of the e/e' phase transition on Au(100) contrasts the relatively sharp transformations observed on both Au(100) and Au(111).[10a,13a] These differences are consistent with the more pronounced nature of the e/e' voltammetric features on Au(110) and (111) seen in Fig. 6. For the Au(110) surface, the phase transition involves the conversion of a noncommensurate near-

hexagonal phase at about −0.05 V to a simpler, approximately (3 × 2), phase exhibiting slightly (0.02–0.03) higher fractional coverages.[11,13b] The reported phase transition on Au(111), occurring at about 0.1 V, features the transformation of a uniaxially compressible (p × √3) phase [approximated on average by (5 × √3] to a rotated hexagonal noncommensurate phase [approximated by (7 × 7)R22° symmetry[10a]], again involving only a slight (0.01–0.02) yet sharp potential-induced coverage increase[13a] (but see footnote 19).

The former transition, in particular, necessitates significant motion of the iodine atoms: most simply, one-half the atoms in the rotated hexagonal arrangement undergo lateral displacement by ca one atomic radius, thereby lining up along the $(1\bar{1}0)$ direction, so to form the (3 × 2) arrangement.[11] The phase transition on Au(111) requires less atomic motion; moreover, the less corrugated nature of the Au(111) versus the Au(110) substrate should provide a smaller kinetic barrier to cooperative adatom motion. These factors account qualitatively for the electrochemically more facile nature of the adlayer phase transition on Au(111) than on Au(110), as can be discerned clearly from the smaller e/e′ voltammetric peak separation, ΔE_p, and peak width, ΔE_W, for the former surface (Fig. 6). Note also the increased ΔE_p values obtained for the faster voltammetric sweep rate (Fig. 6). This shows that obliging the potential-induced phase transition to occur more rapidly requires increased overpotentials in a formally similar fashion to heterogeneous charge-transfer and other potential-(or field-)driven processes.

The differing behavior of the Au(100)–I^- system compared with the other two low-index surfaces is probably due to the geometry of the square-planar lattice favoring closely related adlayer arrangements each featuring iodine rows close to the √2 (R45°) direction. Interestingly, the (2√2 × √2) structure (Fig. 3B) is the only iodine arrangement observed on low-index gold surfaces which feature

an interatomic separation significantly smaller than the iodine van der Waals diameter, 4.3Å. While this $\sqrt{2}$ separation (4.08 Å) necessarily incurs less favorable adsorbate–adsorbate interactions (vide infra), the energetic virtue of the ($2\sqrt{2} \times \sqrt{2}$) arrangement likely occurs from the uniform presence of twofold binding sites (Fig. 3B). The retention of local adlayer regions having the ($2\sqrt{2} \times \sqrt{2}$) arrangement at higher potentials at the cost of forming a structurally nonuniform (spatially mixed) adlayer (Fig. 5A–C) testifies further to the stability of this structure. The generally observed preference for multifold coordination with simple monoatomic adsorbates is clearly evident for the Au(hkl)–I^- systems.[10–12]

Having highlighted the structural dissimilarities between the iodine adlayers on Au(100), (110), and (111), arising clearly from the differing steric factors, it is appropriate to compare the effective iodine packing densities as prescribed most simply by the surface concentration, Γ. The Γ values, obtained by combining the fractional coverages, θ_I, with the substrate atomic densities [1.39, 1.20, and 0.85×10^{15} atoms cm^{-2} for the Au(111), (100), and (110) planes, respectively], exhibit a close similarity. Thus at the electrode potential, E = –0.15 V, for example, the Γ values on (111), (100) and (100) deduced from the coverages given here and in refs. 10, 11, and 13 are 5.4×10^{14}, 5.5×10^{14}, and 5.5×10^{14} atoms cm^{-2}. At 0.15 V, the corresponding Γ values are 6.0×10^{14}, 6.0×10^{14}, and 5.95×10^{14} atoms cm^{-2}. The average adlayer compressibilities (or Γ–E slopes), allowing for the inevitable complications from the occurrence of slight discontinuities in the Γ–E dependence from the phase transitions, are therefore also very similar on the three faces. (This quantity is considered further in the next section.) This observation of closely similar, even near-identical, Γ values on the three low-index faces is perhaps surprising given that the C_d–E data in Fig. 1 show that the onset of iodide adsorption occurs at more negative

potentials on Au(100) and Au(110) than on Au(111). Consequently, the adsorption thermodynamics at low iodide coverages are more favorable at a given electrode potential for Au(100) and (110) than for Au(111).

The latter finding is roughly consistent with the 0.25–0.3 V lower potentials of zero charge ("electrochemical work function") of Au(100) and (110) compared with Au(111) in aqueous media,[22] following the notion that anion chemisorption is being controlled by the metal charge rather than the electrode potential.[23] On the other hand, the near-identical Γ values obtained for ordered iodide adlayers on Au(111) compared with the other two faces at a given electrode *potential* supports the importance of this electrical variable. The latter finding is consistent with the notion that iodide chemisorption on gold can be viewed essentially as a charge-transfer process[4]

$$I^- + \text{Au(surface)} \leftrightarrows \text{I–Au} + e^- \qquad (1)$$

so that the potential-dependent free energy of adsorption is driven chiefly by the electron transfer. Indeed, the potential dependence of the I–Au covalent bond strength appears to be small on the basis of the observed near-invariant gold surface-iodide vibrational stretching frequency over a wide potential range.[4,24]

As might be expected, however, alteration of the electrode metal at similar electrode potentials can result in significantly different iodine packing densities for near-saturated adlayers. For example, a (3 × 3) adlayer (θ_I = 0.44) is observed on Pt(111)[25] and a ($\sqrt{2} \times 5\sqrt{2}$)R45° pattern ($\theta_I$ = 0.6) on Pt(100)[26], both by using in-situ STM at comparable potentials, 0 to 0.5 V vs SCE. These coverages correspond to Γ values of 6.75×10^{14} and 7.9×10^{14} atom cm^{-2}. These larger and more surface orientation-sensitive packing densities on platinum

than on low-index gold surfaces infer the presence of stronger and more site-dependent Pt-I bonding. Similar behavior is observed for iodide adsorption on rhodium low-index surfaces.[21] On Rh(110), for example, a (2 × 7) iodine adlattice can be formed (θ_I = 0.714) which features an iodine interatomic spacing, 3.7 Å, that is noticeably less than the van der Waals diameter.[21] Evidently, then, strong surface-iodine bonding can exert a marked effect on the adlayer packing densities.

Nature of Potential-Dependent Adlayer Interactions

The emergence of such potential-dependent adlayer structural information naturally fuels a desire to describe and eventually understand the nature of the exquisite observed patterns. As for compressed adlayers at ordered metal-uhv interfaces, the structural patterns commonly arise from a fine balance between several energetic factors, and are inadequately understood. One interesting element of the electrochemical systems, however, which is subject to at least a rough analysis concerns the potential-induced adlayer compressibility. This issue has been discussed in particular by the IBM-Almaden group, specifically in connection with accurate spatial adlayer structures for metallic adlayers as provided by SXRS.[5,18,27] They defined for this purpose a two-dimensional isothermal compressibility, κ_{2D}, given by[27]

$$\kappa_{2D} = -a^{-1}(\partial a/\partial \phi)_T \qquad (2a)$$

where a is the area per adlayer atom and ϕ is the two-dimensional spreading pressure. Recasting Eq. (2a) in terms of an electrode potential-dependent surface concentration Γ yields

$$\kappa_{2D} = \Gamma^{-2}(ze)^{-1}(\partial \Gamma/\partial E)_T \qquad (2b)$$

where z is the number of electrons transferred upon adsorption. Assuming that $z \sim 1$ for iodide adsorption (vide supra), for the typical values $(\partial\Gamma/\partial E)_T \sim 1.7 \times 10^{14}$ and $\Gamma \sim 5.5 \times 10^{14}$ atom cm^{-2} observed for the iodine adlayers, from Eq. (2b), we obtain $\kappa_{2D} \sim 6.6 \times 10^{-16}$ cm^2 eV^{-1} (cf ref 13a).

This iodine adlayer compressibility is markedly larger than those obtained for compressed metal adlayers, which vary from about 0.5 to 1.5×10^{-16} cm^2 eV^{-1}.[5,18,27] This difference in the κ_{2D} values is unsurprising: the larger atomic size and more polarizable nature of iodine atoms would be expected to yield more compressible adlayers than for metals. Some insight into the physical factors that influence κ_{2D} for such nonmetallic adlayers can be obtained from an analysis of the various interatomic forces involved. While a full account will be given elsewhere,[28] we briefly summarize here the nature of, and anticipated contributions from, the various types of adsorbate-adsorbate interactions.

Broadly speaking, these fall into five categories. The first arises from the net repulsive interactions between the residual charge on the adsorbate atoms along with the attendant image term at the high coverages, and hence short interatomic distances, characteristic of ordered adlayers.[29] At an interatomic distance r equal to the van der Waals diameter, $d_v = 4.3$ Å, for example, and for a 0.1 e^- charge per adsorbate atom, the calculated energy, W_1, is about 25 meV, varying approximately with r^{-3}. The second term, associated with induced dipole repulsive interactions, is predicted to be unimportant for the present system, contributing only about 1 meV at $r = d_v$. The third energy component, W_3, arising from Lennard-Jones forces, is of course either net attractive or repulsive, depending on r; at $r = d_v$, $W_3 \sim -20$ meV. Even at significantly smaller distances, however, W_3 is predicted to remain attractive: thus at $r = 4.0$ Å, for example, $W_3 \sim -15$ meV. [Note that the smallest r value encountered above, the $\sqrt{2}$ spacing, is slightly larger, 4.08 Å.] The fourth component, generally

associated with nonadditive long-range forces,[29] is also small for interatomic distances comparable to d_v. Thus for $r = d_v$, $W_4 \sim 0.3$ meV, and for $r = 4.0$ Å, $W_4 \sim 6$ meV.

The fifth, and last, anticipated energy component is anticipated to arise from a "substrate-mediated dispersion energy" between adatoms.[29,30] Interestingly, this repulsive component, which scales with r^{-3}, is predicted to provide a predominant contribution to the adlayer interaction energies at interatomic distances close to d_v. Thus at $r = d_v$, $W_5 \sim 60$ meV, and at $r = 4.0$ Å, $W_5 \sim 70$ meV.[29] Overall, the sum of these interaction energies as a function of the adlayer spacing enables estimates of κ_{2D} to be obtained, provided that the adsorbate-substrate bonding interactions remain approximately unchanged. This procedure yields, for example, $\kappa_{2D} \sim 8 \times 10^{-16}$ cm^2 eV^{-1} at $r = d_v$. While this estimate is comparable to the measured values, the former increase markedly towards larger r; for example, $\kappa_{2D} \sim 20 \times 10^{-16}$ cm^2 eV^{-1} for $r = 4.6$ Å.[29] This tendency to overestimate κ_{2D}, however, is not unexpected given the simplified nature of the calculational model. For example, as seen above, iodine adlayer compression results inevitably in an increased occupancy of lower coordination binding sites relative to the preferred multifold geometries. This factor should therefore diminish the average adsorbate-surface binding energy, and therefore destabilize the system further towards higher packing densities, thereby decreasing κ_{2D}.

CONCLUDING REMARKS

Together with our earlier and companion reports,[10-12] the present study demonstrates the capability of in-situ STM for adding a remarkable degree of atomic-level insight into the potential-dependent double-layer behavior of an archetypical anion adsorbate system: iodide at ordered gold-aqueous interfaces.

This coupled examination of anion adlayer structure and dynamics as a function of electrode potential and crystallographic orientation provides, we believe, the most comprehensive picture of anion adsorption on metal electrodes attained to date. The classic electrochemical studies of adsorption on ordered gold and silver electrodes undertaken by Hamelin demonstrated in a macroscopic fashion the marked influence of the substrate crystallographic orientation.[22] The new-found ability of STM to uncover the microscopic structural and dynamical factors responsible for this exquisite sensitivity seems poised to enrich our appreciation of adsorptive double-layer properties, of longstanding importance in electrochemistry, across a broader perspective at the atomic level.

More specifically, the adlayers formed in the present Au(100)-I system feature an intriguing form of real-space "structural heterogeneity" which, to our knowledge, has not been discussed previously either for electrochemical or uhv-based adlayer systems. The observed erratic variations in the atomic adlayer patterns seen even on uniform substrate terraces (Fig. 5A-C) may be rationalized on entropic grounds, provided that the local structurally distant adlayer regions are thermodynamically almost isoenergetic. It will be interesting to see if related behavior, rather than the now-common observation of microscopically uniform adlayer arrangements, appear in other electrochemical systems.

The ability to discover such local, even irregular, variations in atomic or nanoscale structure is a hallmark of STM which sets it apart from diffraction-based methods such as SXRS which sense only structural features associated with repetitive order. On the other hand, the SXRS measurements of Ocko et al on the Au(111)-I and Au(110)-I electrochemical systems[13] provide a persuasive testament to the remarkably accurate spatial information attainable by this approach. While the use of composite-domain imaging tactics along with the receipt of z-corrugation (moiré) patterns can largely circumvent the problems of x-y

distortions in STM data, the structural data provided by SXRS are still unquestionably of higher accuracy. Nonetheless, a comforting feature (for now!) of the corresponding STM and SXRS data for the Au(111)-I and Au(110)-I systems is that they are largely in good or even excellent agreement. Although this circumstance, also seen for other adlayer systems,[31] is unlikely to be generally true, its occurrence adds substance to the notion that STM (and other probe microscopies) along with SXRS should be of inherently complementary value to the rapidly developing discipline of in-situ electrochemical surface science.[4]

ACKNOWLEDGEMENTS

We are thankful to Antoinette Hamelin for preparing the gold single crystals used here, and to Jia Wang and Ben Ocko for sharing their SXRS data prior to publication. F-C.L. was supported at Purdue by the Purdue-USTC Scholar Exchange Program. This work is supported by the Office of Naval Research and the National Science Foundation.

REFERENCES AND NOTES

1) For example: Ohtani, H., Kao, C-T., Van Hove, M.A., and Somorjai, G.A., Prog. in Surf. Sci., 1986, 23, 155.

2) (a) Hubbard, A.T., Chem. Revs., 1988, 88, 633; (b) Soriaga, M., Prog. in Surf. Sci., 1992, 39, 325.

3) (a) Sass, J.K. and Bange, K.J., ACS Symp. Ser., 1988, 378, 54; (b) Wagner, F.T., in "Structure of Electrified Interfaces", Lipkowski, J. and Ross, P.N., eds., VCH Publishers, New York, 1993. Chapter 9.

4) Weaver, M.J. and Gao, X., Ann. Rev. Phys. Chem., 1993, 44, 459.

5) Toney, M.F. and Melroy, O.R., in "Electrochemical Interfaces: Modern Techniques for In-Situ Interface Characterization", Abruña, H.D., ed., VCH Publishers, New York, 1991, Chapter 2.

6) (a) Gao, X., Hamelin, A., and Weaver, M.J., Phys. Rev. Lett., 1991, 67, 618; (b) Gao, X., Hamelin, A., and Weaver, M.J., Phys. Rev. B, 1992, 46, 7096; (c) Gao, X., Edens, G.J., Hamelin, A., and Weaver, M.J., Surf. Sci., 1993, 296, 333; (d) Gao, X. and Weaver, M.J., J. Phys. Chem., 1993, 97, 8685.

7) Gao, X., Hamelin, A., and Weaver, M.J., J. Phys. Chem., 1991, 95, 6993.

8) (a) Gao, X., Hamelin, A., and Weaver, M.J., Phys. Rev. B, 1991, 44, 10983; (b) Gao, X. and Weaver, M.J., Surf. Sci., submitted.

9) (a) Gao, X., Edens, G.J., Hamelin, A., and Weaver, M.J., Surf. Sci., submitted; (b) Gao, X., Hamelin, A., and Weaver, M.J., Surf. Sci., 1992, 274, L588.

10) (a) Gao, X. and Weaver, M.J., J. Am. Chem. Soc., 1992, 114, 8544; (b) Haiss, W., Sass, J.K., Gao, X., and Weaver, M.J., Surf. Sci., 1992, 274, L593.

11) Gao, X., Edens, G.J., and Weaver, M.J., J. Phys. Chem. (companion paper to present manuscript).

12) Gao, X. and Weaver, M.J., Ber. Bunsenges. Phys. Chem., 1993, 97, 507.

13) (a) Ocko, B.M., Watson, G.M., and Wang, J., J. Phys. Chem., 1994, 98, 897; (b) Ocko, B.M. and Wang, J., in preparation.

14) Gao, X. and Weaver, M.J., Phys. Rev. Lett., submitted.

15) As before,[10,11] one can perceive the ordered adlayers to consist of monoatomic iodine atoms rather than iodide ions since adsorbed iodide on gold commonly appears to feature largely complete charge donation (or charge sharing). This is deduced partly on the basis of the near-unity values of the electrosorption valency measured for low-coverage disordered adlayers from a thermodynamic analysis of capacitance-potential data,[16] and for high-coverage ordered adlayers on Au(111) from SXRS measurements.[13a]

16) Edens, G.J., unpublished results

17) Gordon, A.J., Ford, R.A., "The Chemist's Companion", Wiley, New York, 1972, p. 109.

18) Toney, M.F., Gordon, J.G., Samant, M.G., Borges, G.L., Melroy, O.R., Kau, L-S., Wiesler, D.G., Yee, D., and Sorenson, L.B., Phys. Rev. B, 1990, 42, 5594.

19) Under some conditions, especially for Au(111) crystals having large uniform terraces, large iodine adlayer domains having (3 × 3) symmetry are observed by STM, a markedly different structure to that reported in ref. 10 and 13a. The iodine rows are observed to lie along the substrate direction, the z-corrugations suggesting alternate atop and twofold bridging sites. This adlayer, having $\theta_I = 0.44$, was reported earlier by Tao and Lindsay.[20] Further details and discussion will be given elsewhere.[21]

20) Tao, N.J. and Lindsay, S.M., J. Phys. Chem., 1992, 96, 5213.

21) Gao, X. and Weaver, M.J., to be published.

22) Hamelin, A., in "Modern Aspects of Electrochemistry", Vol. 16, Conway, B.E., White, R.E., and Bockris, J.O'M., eds., Plenum, New York, 1985, Chapter 1.

23) Parsons, R., J. Electroanal. Chem., 1963, 7, 136; 8, 93.

24) Gao, P. and Weaver, M.J., J. Phys. Chem., 1986, 90, 4057.

25) Yau, S-L., Vitus, C.M., Schardt, B.C., J. Am. Chem. Soc., 1990, 112, 3677.

26) a) Vitus, C.M., Chang, S-C., Schardt, B.C., Weaver, M.J., J. Phys. Chem. 1991, 95, 7559; (b) Vitus, C.M., Ph.D. thesis, Purdue University, 1991.

27) Melroy, O.R., Toney, M.F., Borges, G.L., Samant, M.G., Kortright, J.B., Ross, P.N., Blum, L., Phys. Rev. B, 1988,38, 10962.

28) Liu, F-C., Gao, X., Weaver, M.J., to be published.

29) a) Bruch, L.W., Surf. Sci., 1983, 125, 194; (b) Bruch, L.W., Cohen, P.I., Webb, M.B., Surf. Sci., 1976, 59,1.

30) McLachlan, A.D., Mol. Phys., 1964, 7, 381.

31) Chen, C.H., Kepler, K.D., Gewirth, A.A., Ocko, B., Wang, J., J. Phys. Chem., 1993, 97, 7290.

FIGURE CAPTIONS

Fig 1

A-C) Cyclic voltammograms (10 mV s^{-1}, solid traces) and differential capacitance-potential (C_d-E) data (10 mV s^{-1} dashed traces) obtained in 50 mM $KClO_4$ + 5 mM KI for: A) Au(111); B) Au(100); C) Au(110), showing the various phase transitions induced by iodide adsorption.

Fig 2

Atomic-resolution STM images obtained for Au(100) in 10 mM KI, showing "low-potential" ordered iodine adlayer. A) Mildly filtered composite-domain substrate/adlayer image, with potential stepped from -0.25 V to -0.1 V one third along upward-rastered image acquisition, showing substrate-adlayer atomic registry for approximately ($2\sqrt{2} \times 11\sqrt{2}$) iodine adlayer. B) Height-shaded image of slightly compressed adlayer I, approx ($2\sqrt{2} \times 15\sqrt{2}$). C,D) Top-view large-scale images of compressed ($2\sqrt{2} \times p\sqrt{2}$) adlayer I obtained at 0.05 V, with p = 20-25.

Fig 3

A-C) Schematic ball-model structures of ordered Au(100)-I unit cells considered here.

Fig 4

A) Composite-domain substrate/adlayer image, generated by stepping substrate potential from -0.25 to 0 V during upward-rastered image acquisition yielding ($2\sqrt{2} \times \sqrt{2}$) iodine adlayer. B,C) Large-scale images of ($2\sqrt{2} \times \sqrt{2}$) adlayer, obtained at 0.05 V, showing adjoining rotational domains and "mobile iodine channel" regions, respectively (see text). D) Composite-domain image, formed by stepping potential from -0.25 to 0.3 V during upward-rastered data acquisition, showing formation of high-potential adlayer III.

Fig 5

A-C) STM images of high-potential iodine adlayers on Au(100) at 0.2 V, showing atomic heterogeneities. D) For same surface region as C, but after altering potential to 0 V, showing effect on substrate from ridged iodine strings.

Fig 6

Left-hand side: Cyclic voltammograms for Au(111), (100), and (110), as indicated, within potential regions corresponding to iodine adlayer transitions (see text). Electrolyte was 50 mM $KClO_4$ + 5 mM KI. Dashed and solid traces are 5 and 50 mV s^{-1} sweep rates, respectively. Right-hand side: corresponding differential capacitance-potential curves, obtained at 5 mV s^{-1}, with 10 mV p-p 23 Hz ac signal.

Fig 7

Sequence of potentiodynamic STM images, obtained at 5 mV s^{-1}, showing "semi-continuous" changes in iodine adlayer structure occurring under voltammetric conditions. A) Downward-rastered image, from 0.1 to 0 V vs SCE; B) Upward-rastered image, from -0.02 to 0.12 V; C) Downward-rastered, from -0.12 to -0.22 V. D) Upward-rastered image, during return (positive-going) potential sweep, from 0 to 0.1 V, showing hysteresis in comparison with A (see text).

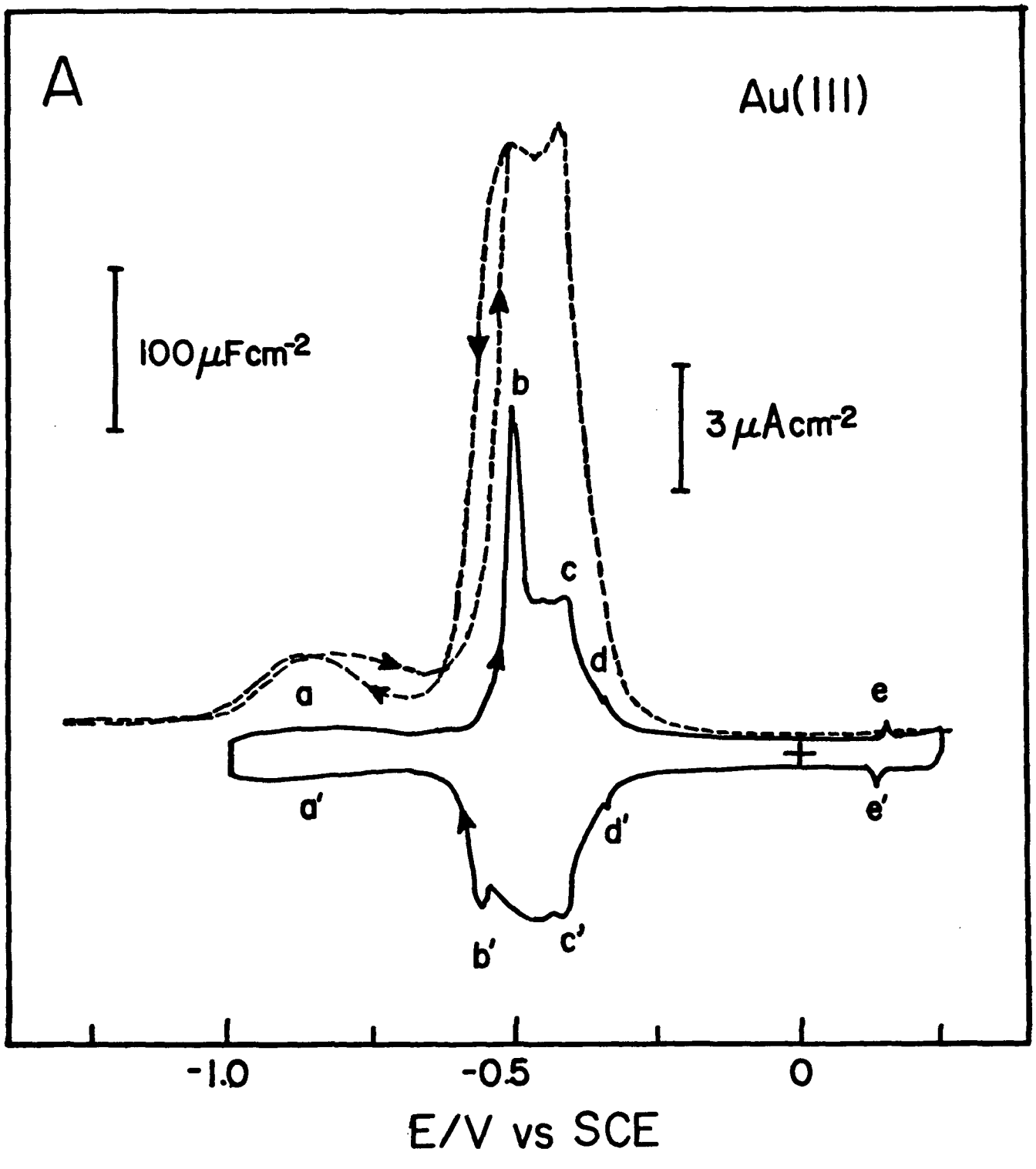

FIG 1A

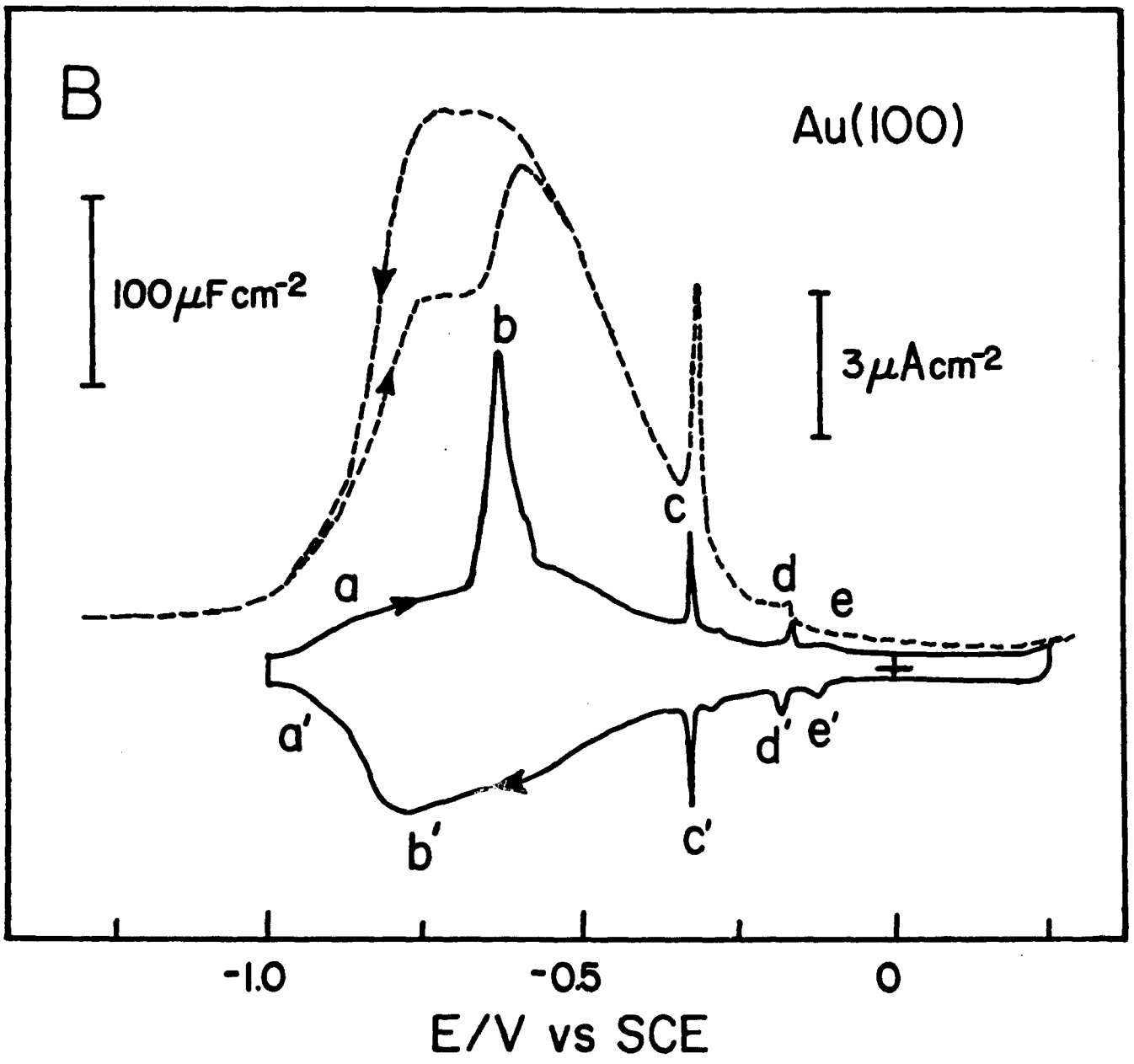

FIG 1B

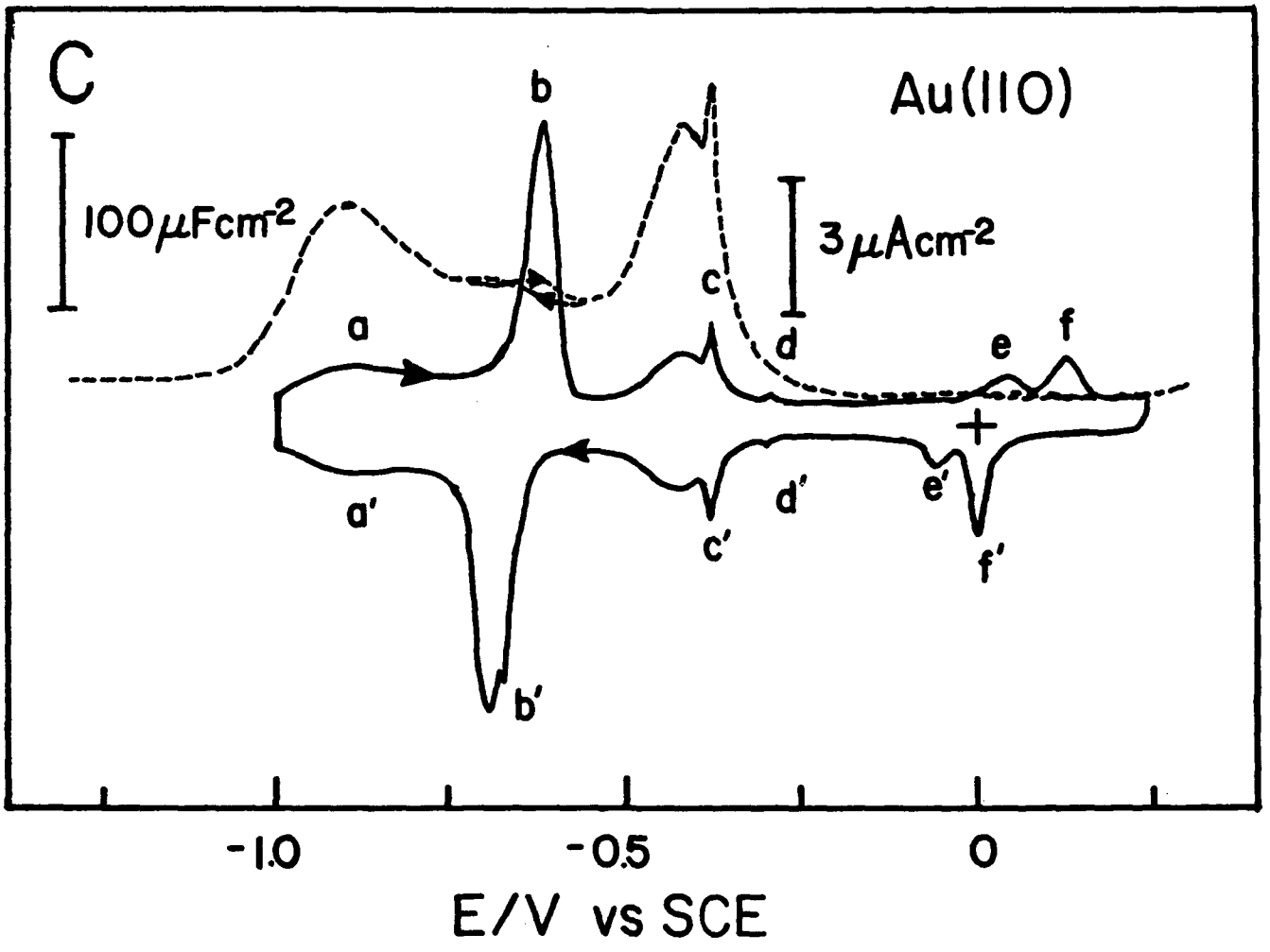

FIG 1C

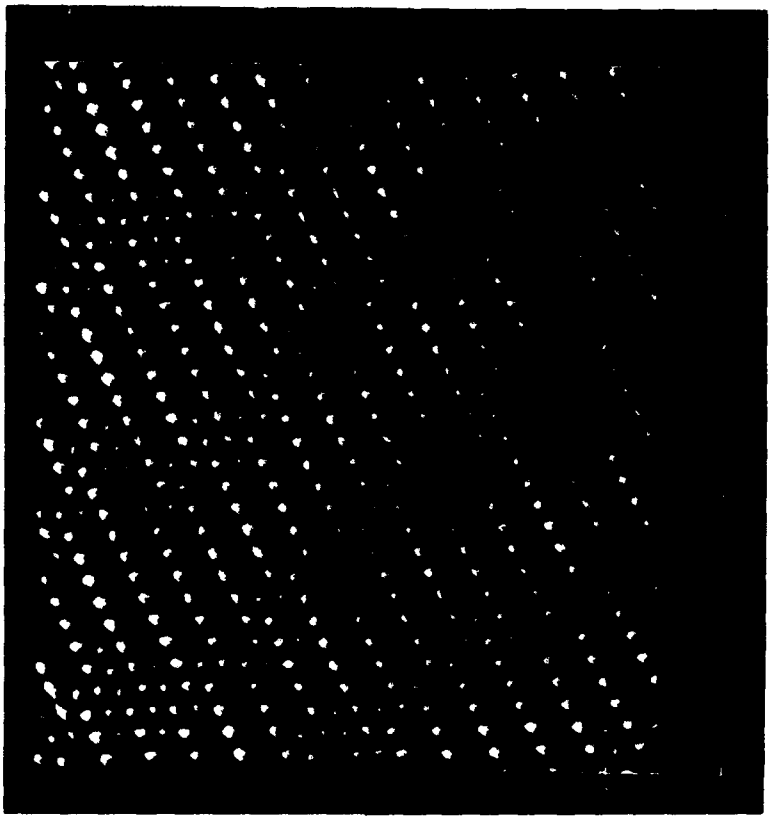

B

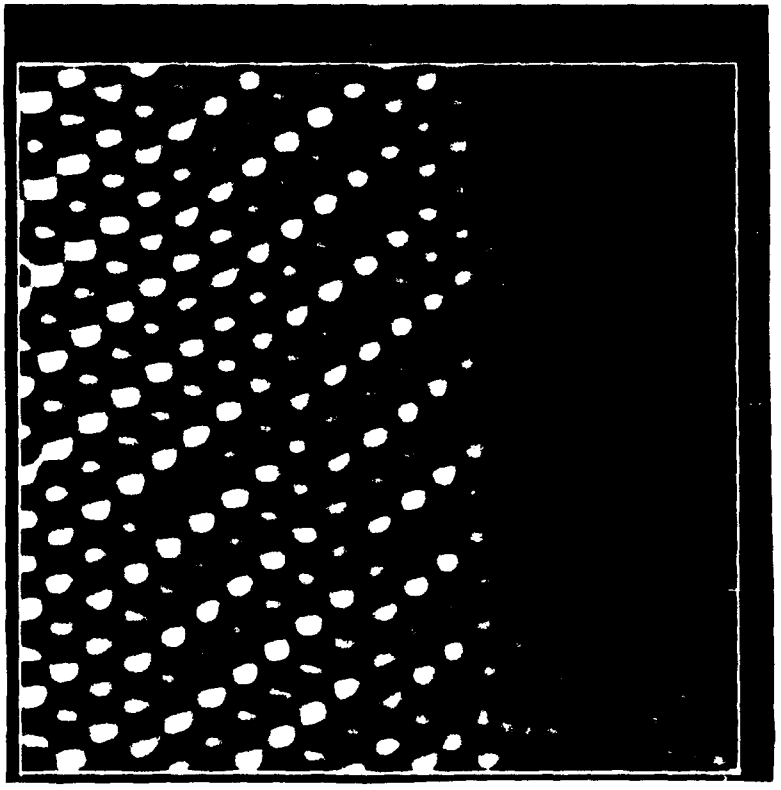

A

FIG 2

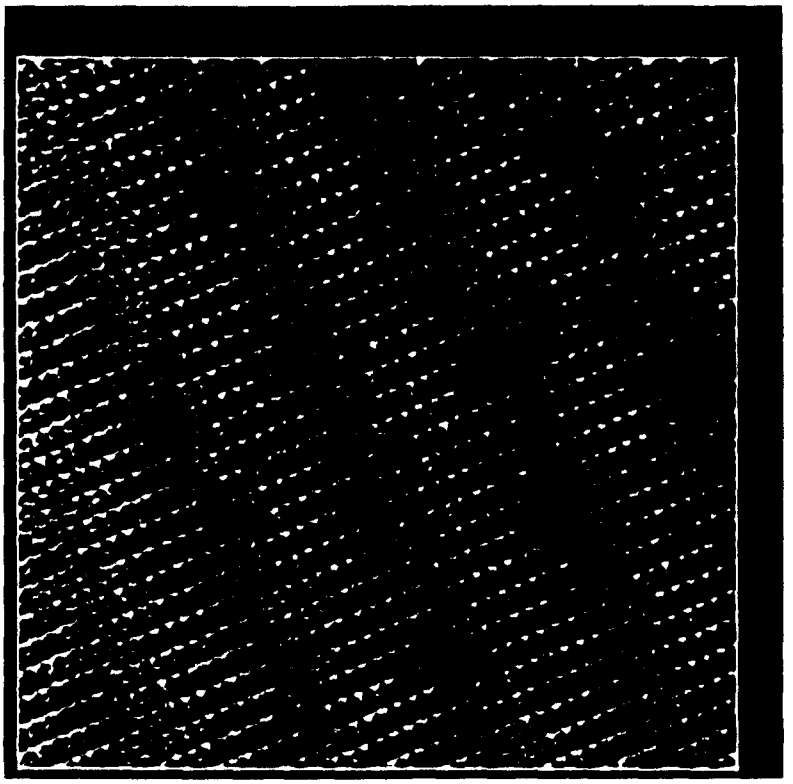

A

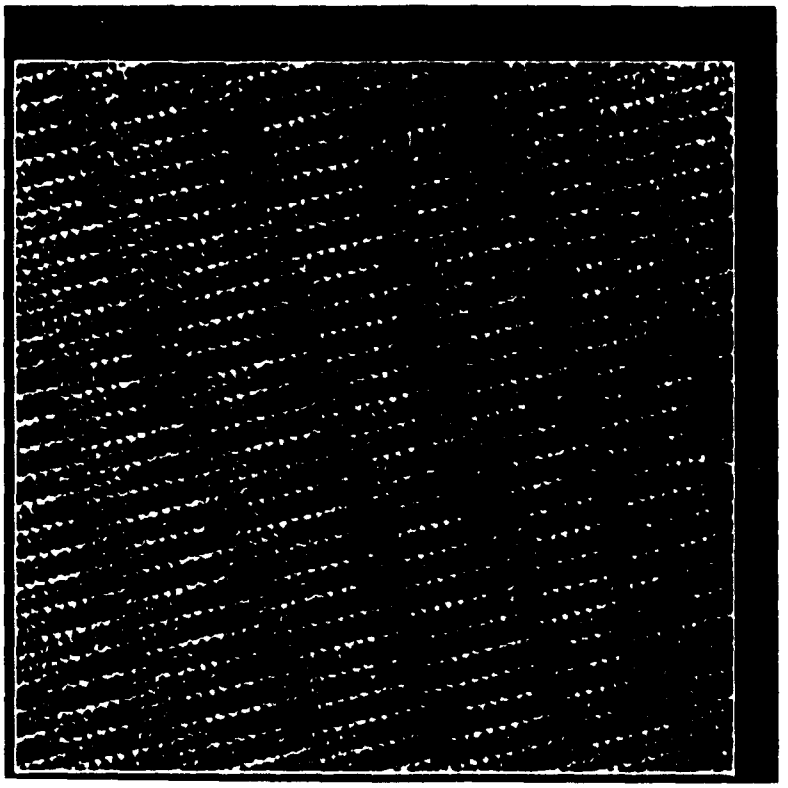

C

FIG 2 (CONTD)

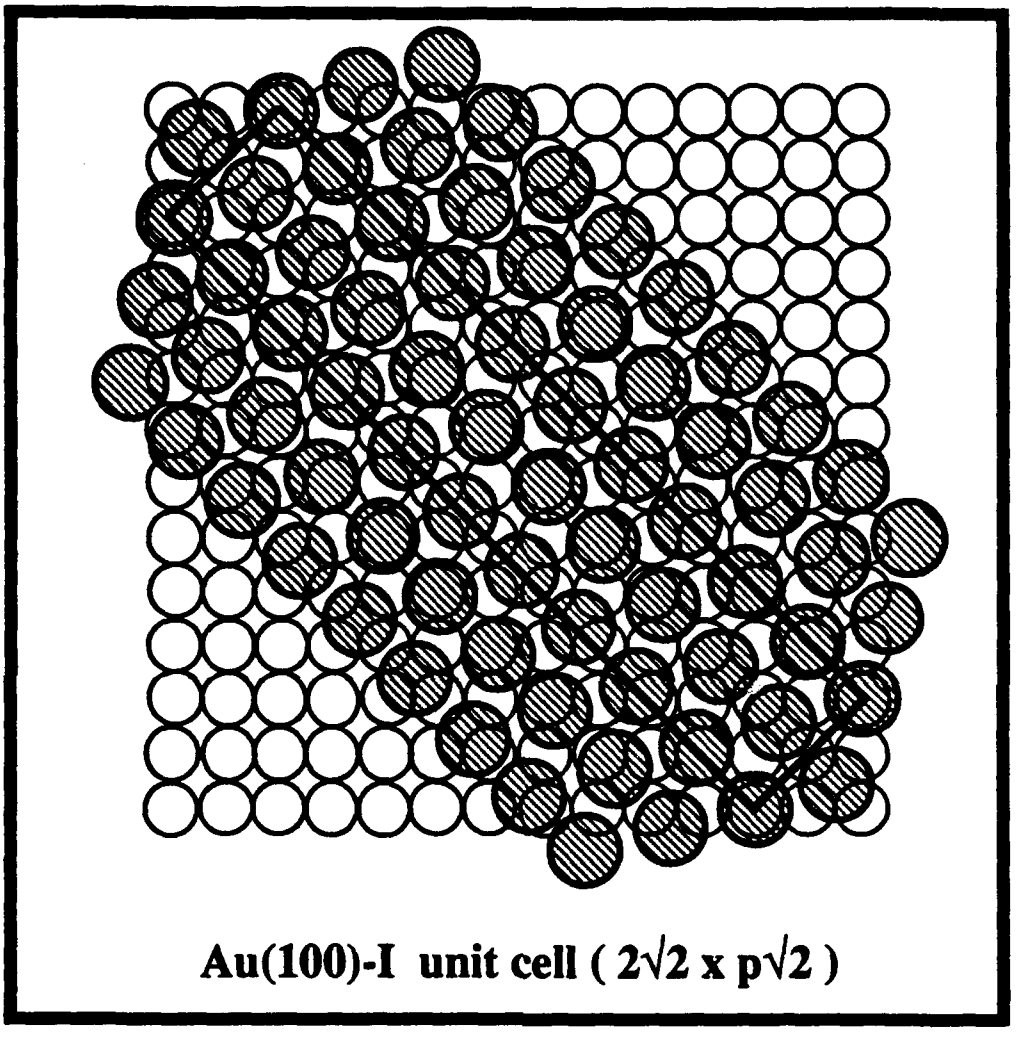

Au(100)-I unit cell (2√2 x p√2)

FIG 3A

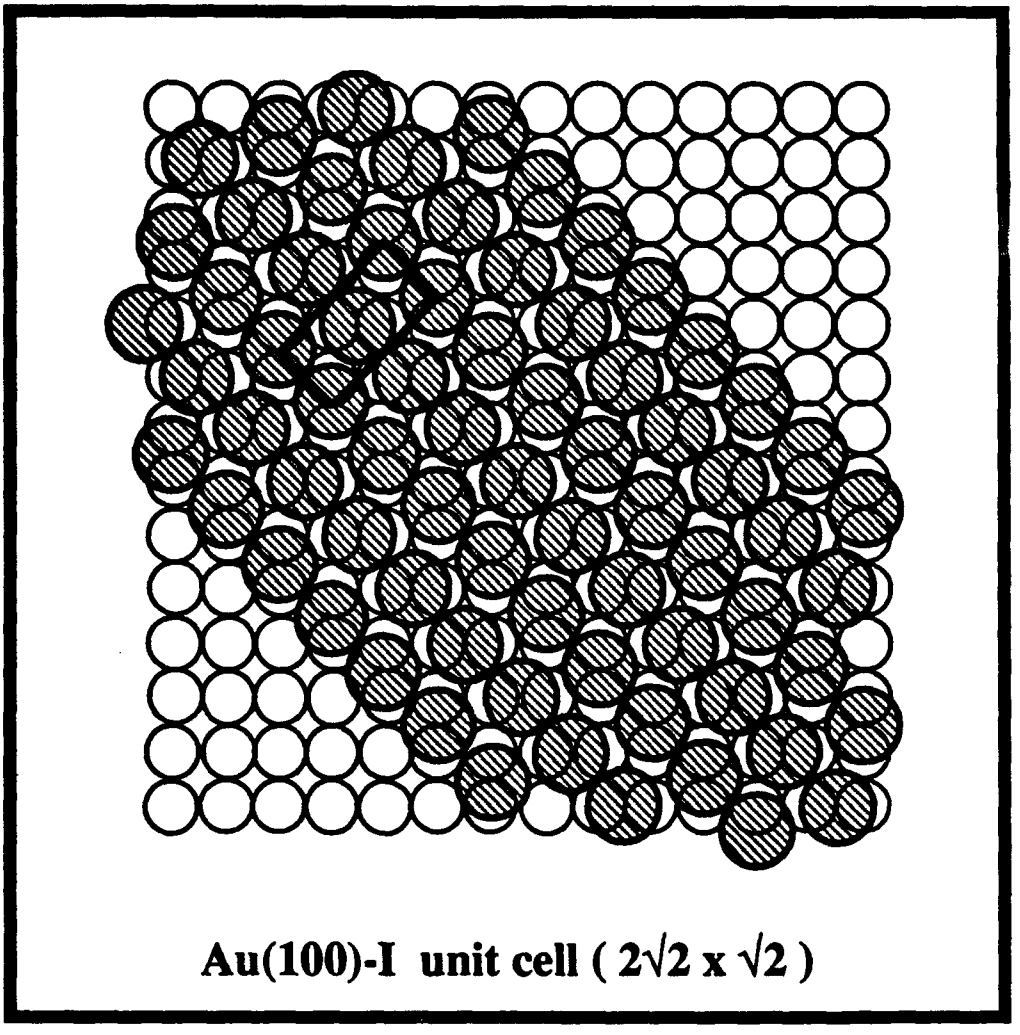

Au(100)-I unit cell ($2\sqrt{2}$ x $\sqrt{2}$)

FIG 3B

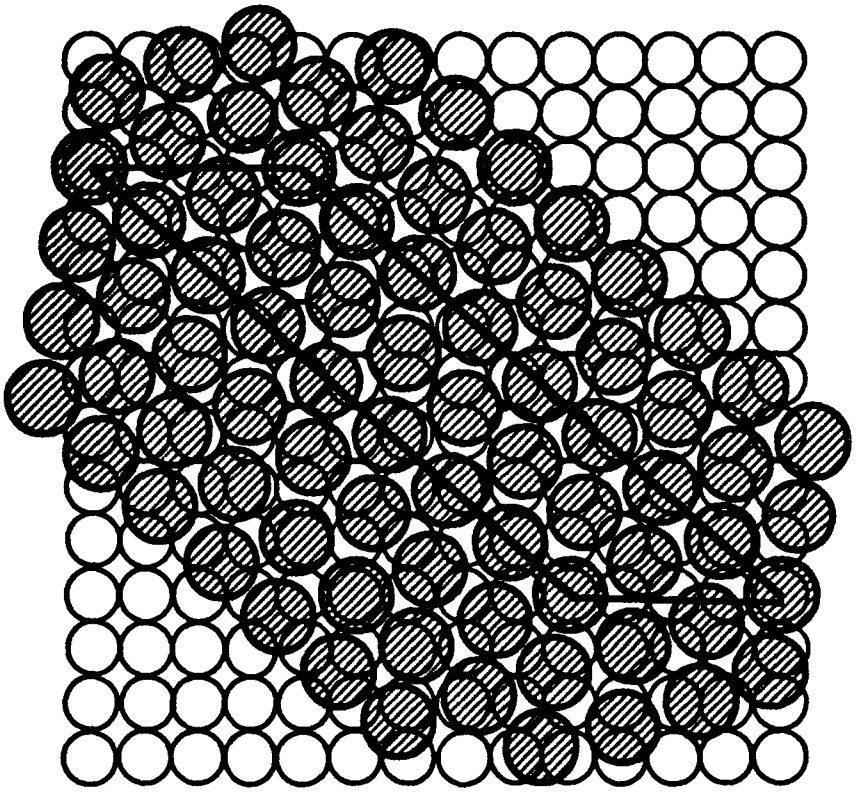

Au(100)-I unit cell (4 x √129)

FIG 3C

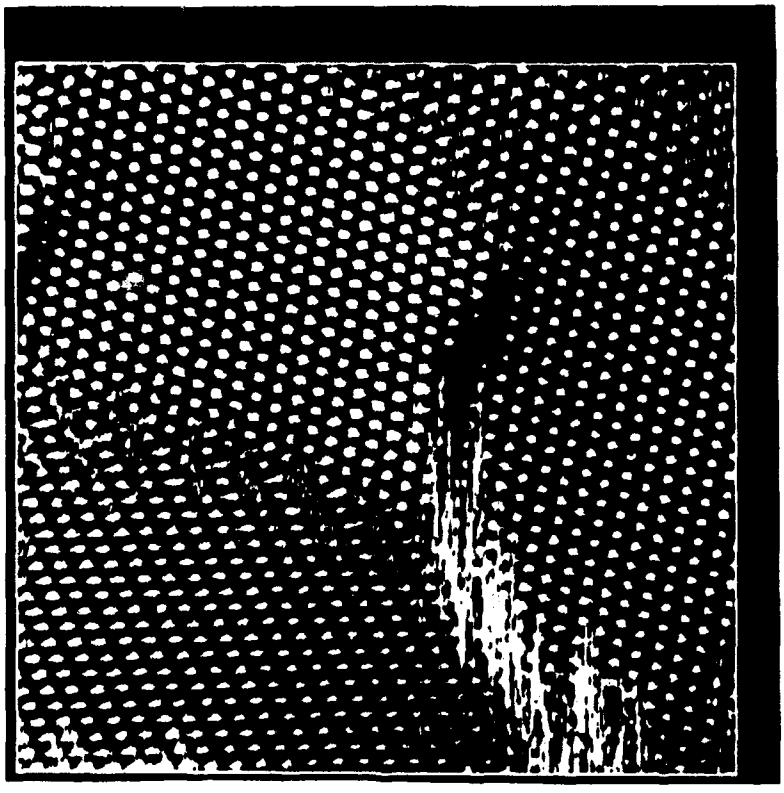

B

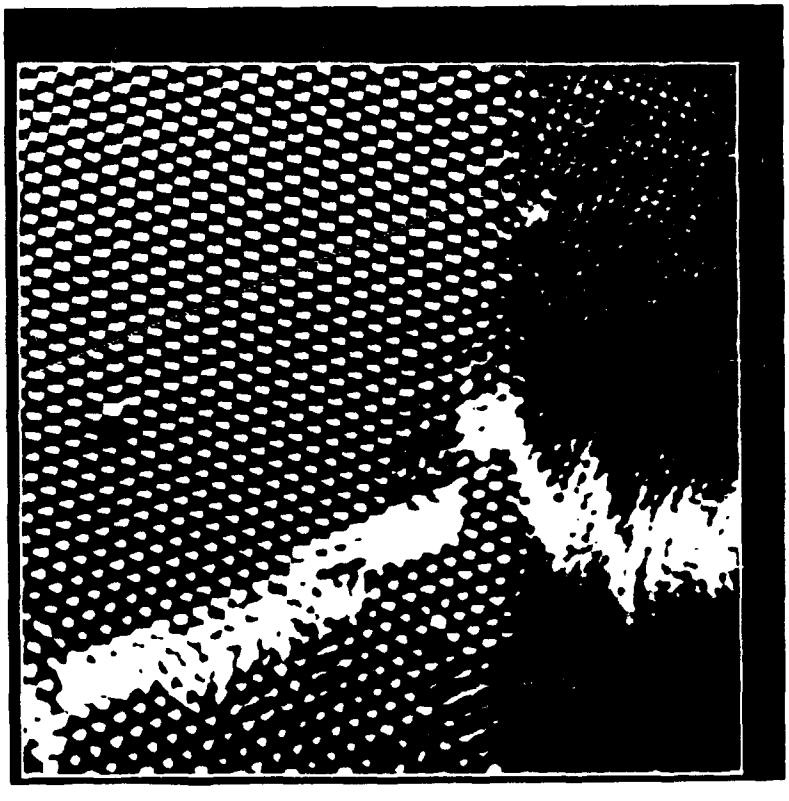

A

FIG 4

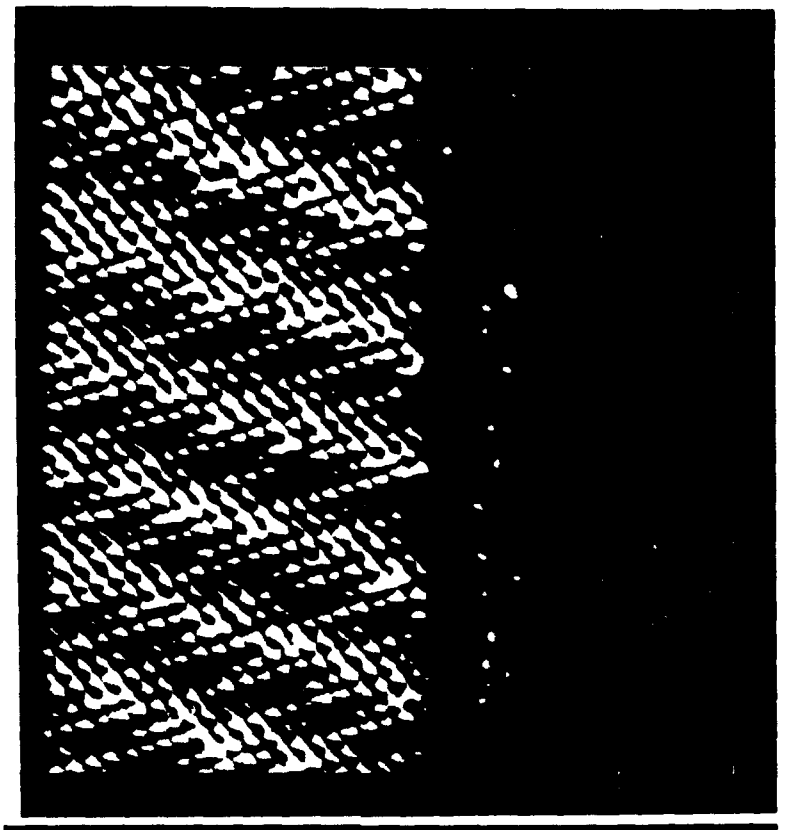

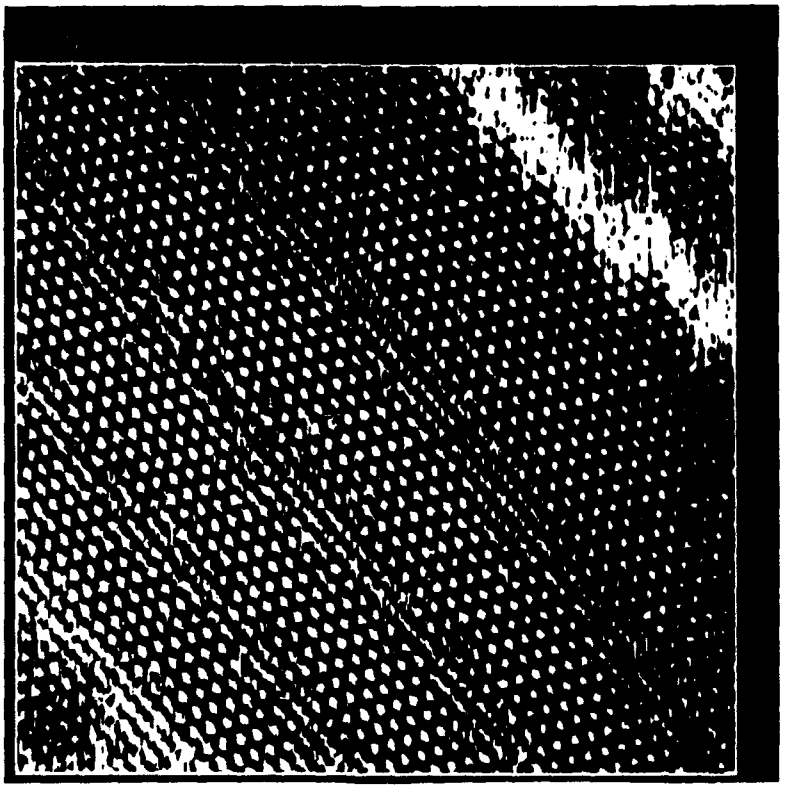

FIG 4 (CONTD)

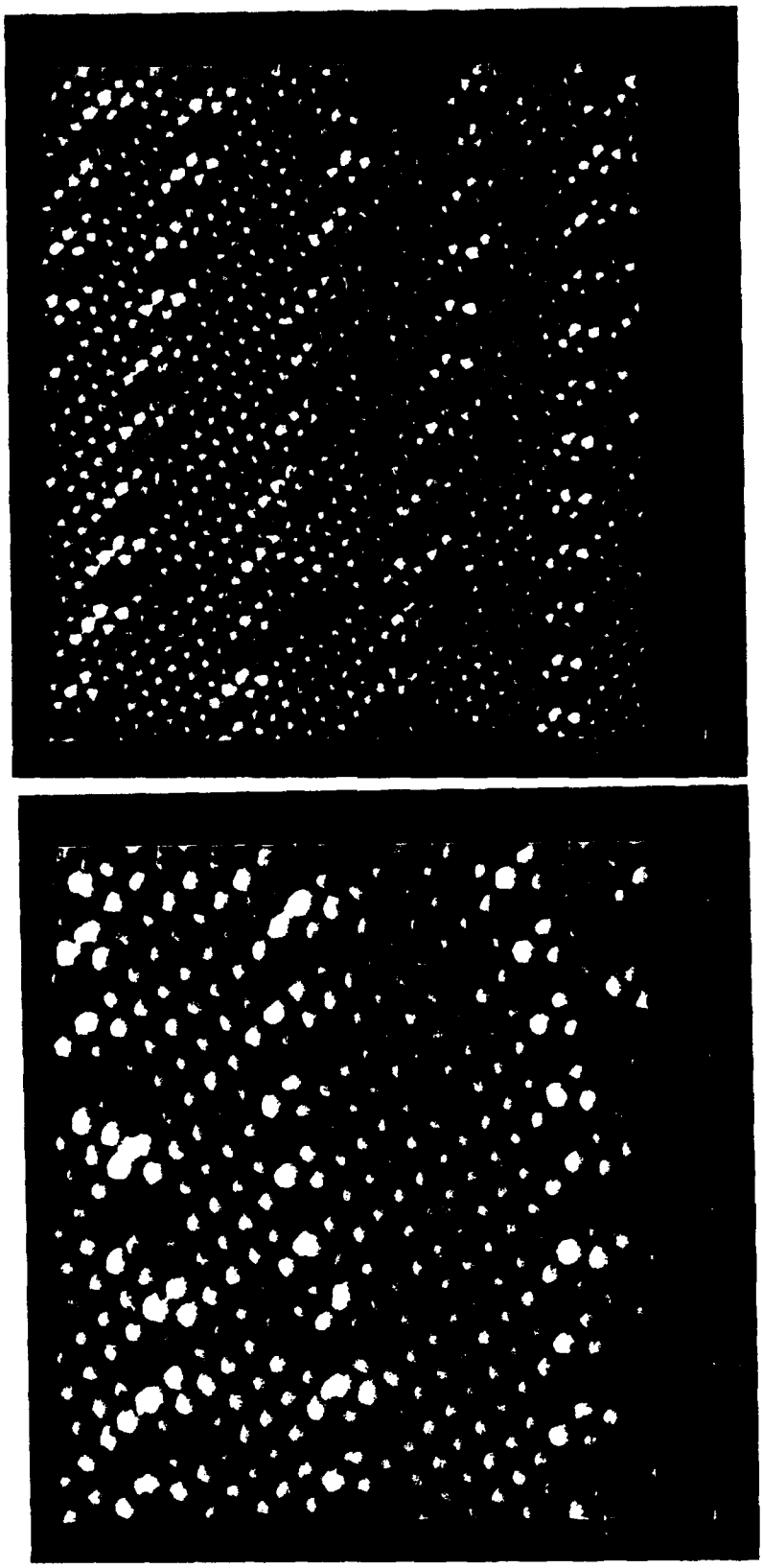

FIG 5

A

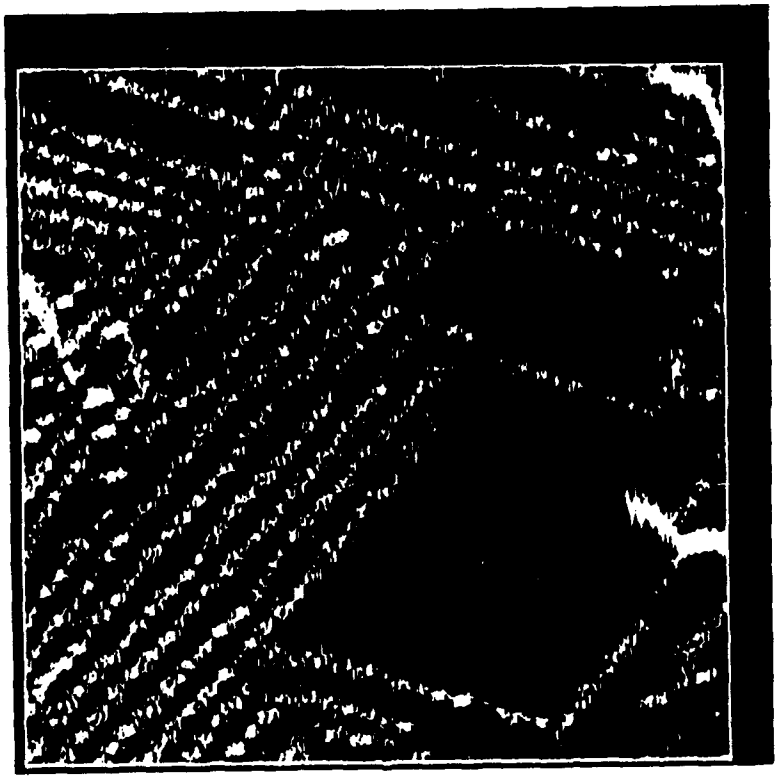

C

FIG 5(CONTD)

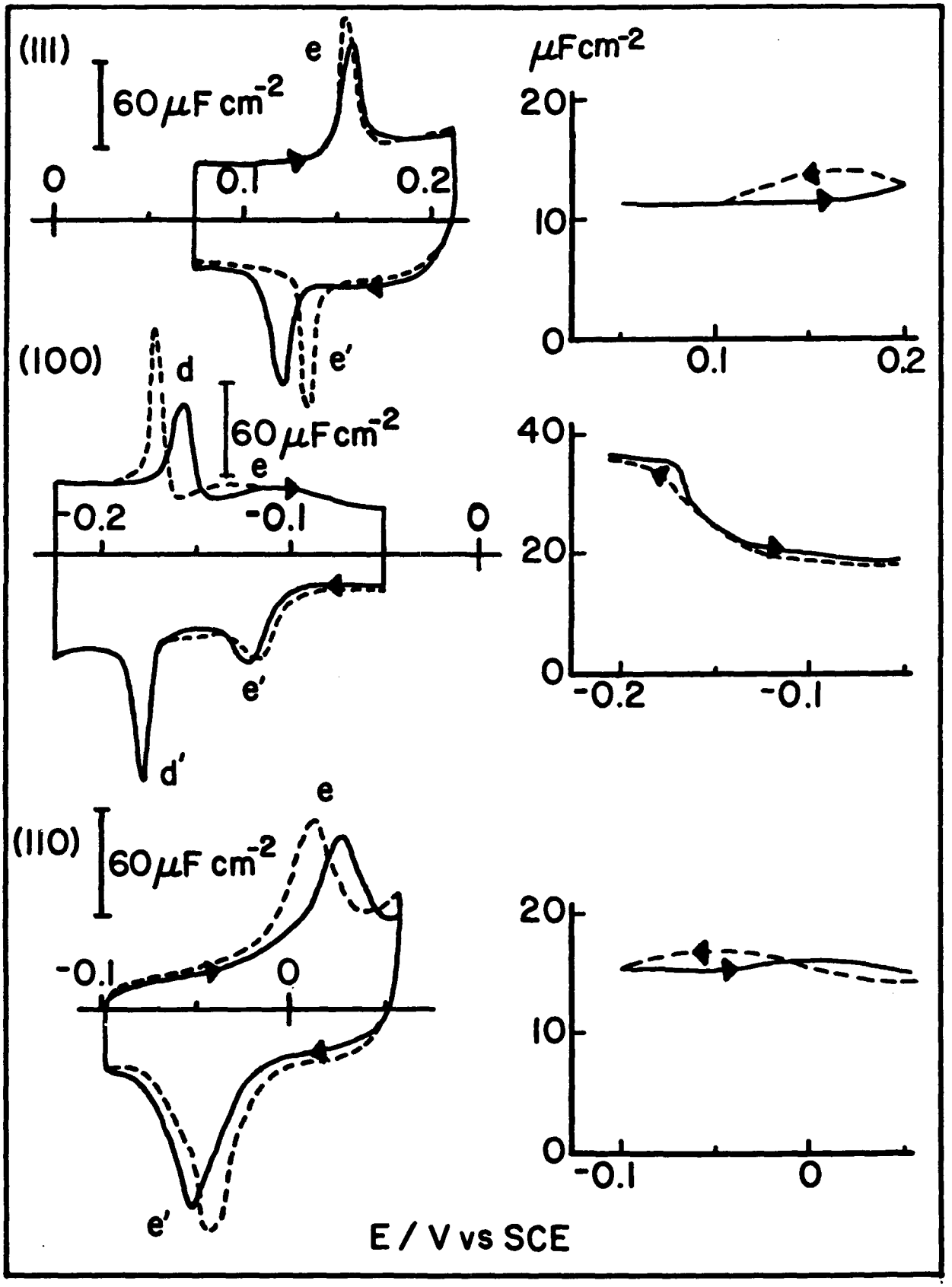
(111)
60 μF cm⁻²
e
e'
0
0.1
0.2
μF cm⁻²
20
10
0
0.1
0.2
(100)
d
60 μF cm⁻²
e
e'
d'
-0.2
-0.1
0
40
20
0
-0.2
-0.1
(110)
60 μF cm⁻²
e
e'
-0.1
0
20
10
0
-0.1
0
E / V vs SCE

FIG 6

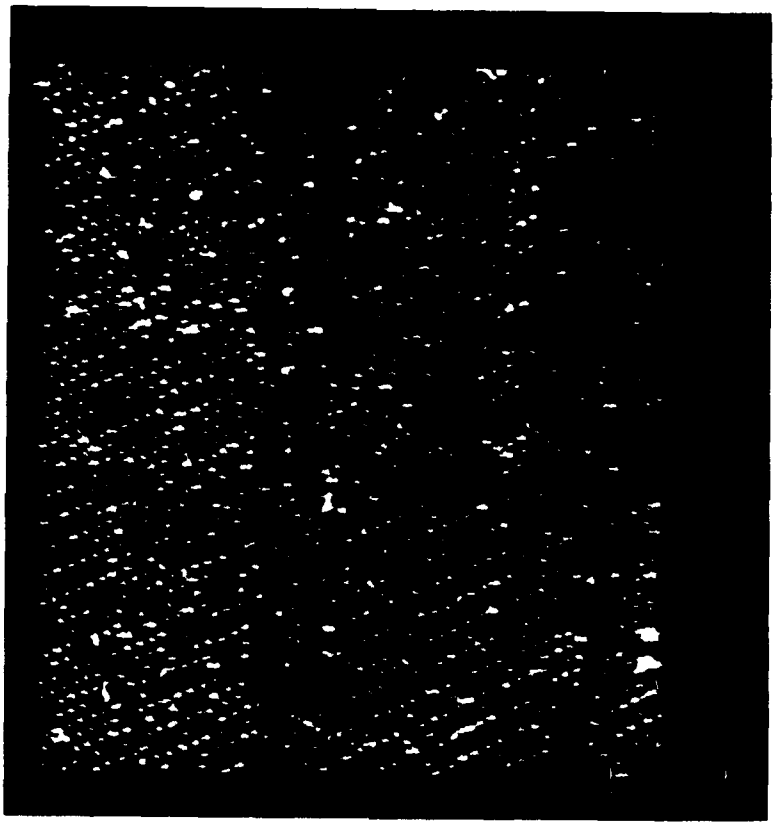

B

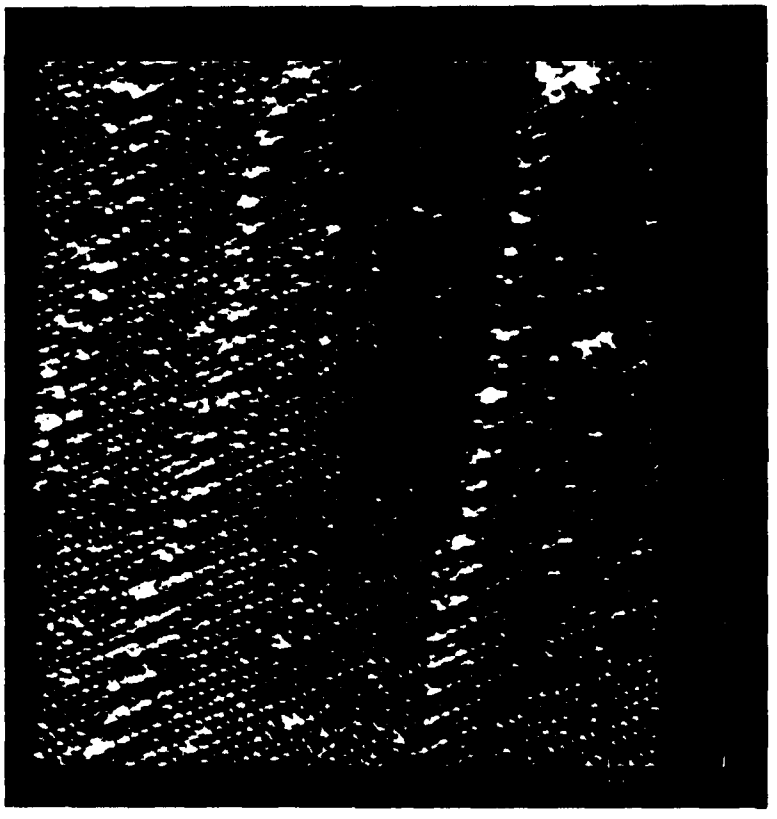

A

FIG 7

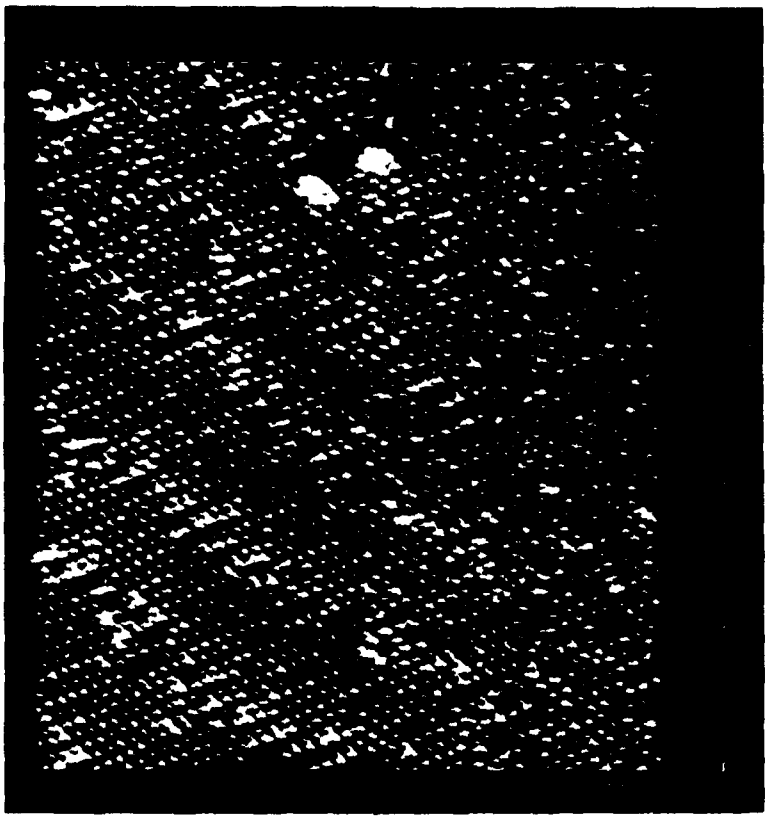

A

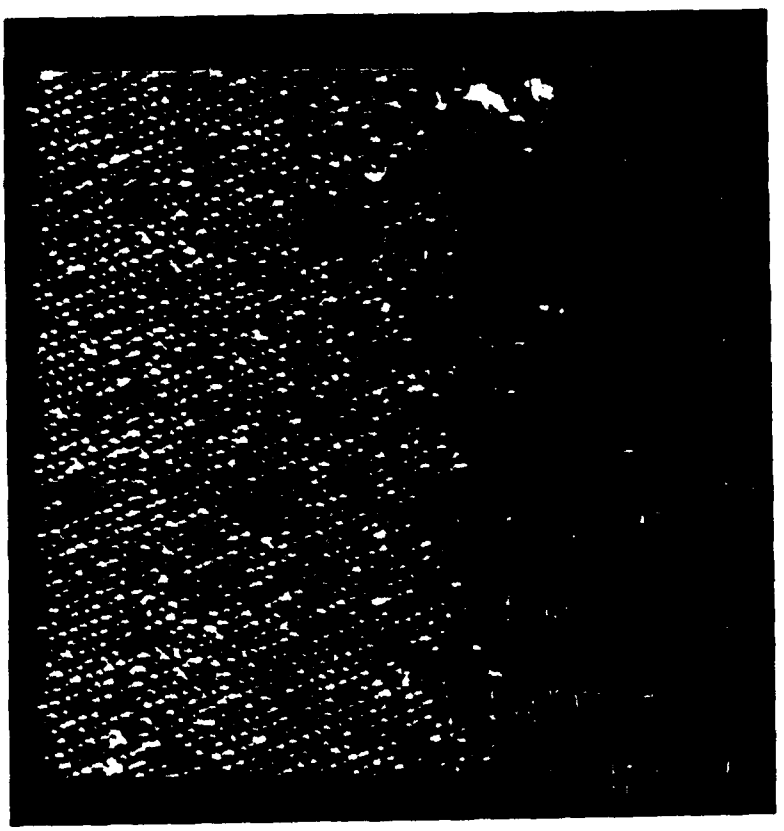

C

FIG 7 (CONTD)